Research Square

Preprints are preliminary reports that have not undergone peer review.
They should not be considered conclusive, used to inform clinical practice,
or referenced by the media as validated information.

Impact of Dual-Source Spectral Shaping Technology (100/Sn150 kV) on Radiation Dose and Image Quality in Orbital CT

Zixuan Ma
Beijing Tongren Hospital Department of Radiology
Zechen Feng
Beijing center for disease control and prevention
Wei Li
Beijing Tongren Hospital Department of Radiology
Yuhe Cheng
Beijing Tongren Hospital Department of Radiology
Wentao Ma
Beijing Tongren Hospital Department of Radiology
Yongxian Zhang
Beijing Tongren Hospital Department of Radiology
Yantao Niu
Beijing Friendship Hospital Department of Radiology
Dandan Liu
trdandan4170@163.com

Beijing Tongren Hospital Department of Radiology

Research Article

Keywords: Dual-Source Spectral shaping technology, Computed tomography, Orbit, Image quality, Radiation dose

Posted Date: February 26th, 2026

DOI: https://doi.org/10.21203/rs.3.rs-8557208/v1

License: This work is licensed under a Creative Commons Attribution 4.0 International License.
Read Full License

Additional Declarations: No competing interests reported.

Impact of Dual-Source Spectral Shaping Technology (100/Sn150 kV) on Radiation Dose and Image Quality in Orbital CT

Zixuan Ma[a], Zechen Feng[b], Wei Li[a], Yuhe Cheng[a], Wentao Ma[a], Yongxian Zhang[a], Yantao Niu[c], Dandan Liu[a]*

[a]From the Department of Radiology, Beijing Tongren Hospital, Capital Medical University, Beijing, China.

[b]From Beijing center for disease control and prevention, Beijing, China.

[c]From the Department of Radiology, Beijing Friendship Hospital, Capital Medical University, Beijing, China.

*Correspondence:

Dandan Liu

trdandan4170@163.com

Abstract

Background: This study investigates the impact of dual-source spectral shaping (DSSS) technology on radiation dose and image quality in orbital CT.

Methods: A head phantom and the Catphan 600 were scanned using a dual-source CT scanner under a conventional protocol (Group A: 120 kV, $CTDI_{vol}$ = 28.4 mGy) and a DSSS protocol (100/Sn150 kV, Group B: with $CTDI_{vol}$ matching Group A; Group C:84% of Group A's $CTDI_{vol}$). Lens doses were measured using thermoluminescent dosimeters, and CT values were recorded. Noise power spectrum (NPS), task-based transfer function (TTF) and detectability index (d′) were calculated. A total of 160 orbital CT examinations were randomly selected, performed under the conventional (Group A) or DSSS protocol(Group C). DLP, scanning length, lens dose, contrast-to-noise ratio (CNR) and gray-scale standard deviation were recorded. Two radiologists evaluated the images using a double-blind method on a 5-point scale.

Results: In the phantom study, Group C showed significantly lower lens dose than Groups A and Group B (P = 0.004). Significant differences in CT values, $MTF_{50\%}$ and $MTF_{10\%}$ were observed between Group A and both Groups B and C (P < 0.001). No significant difference in d' was found among the three groups (P = 0.830). In the clinical study, the DSSS protocol resulted in significantly lower lens dose and gray-scale standard deviation compared to the conventional protocol, while CNR increased (P < 0.001). Subjective image scores for DSSS were all ≥ 4 points.

Conclusion: DSSS technology can significantly reduces lens dose and improves image quality in orbital CT.

Key words: Dual-Source Spectral shaping technology; Computed tomography; Orbit; Image quality; Radiation dose

Abbreviations

CNR	Contrast to noise ratio
$CTDI_{vol}$	Volume CT dose index
CTP	Catphan
DLP	Dose-length product
DSSS	Dual-source spectral shaping
d′	Detectability Index
MTF	Modulation Transfer Function
NPWE	Non-Prewhitening with Eye filter
NPS	Noise Power Spectrum
OBTCM	Organ-based tube current modulation
ROI	Regions of interest
TLD	Thermoluminescent dosimeter
TTF	Task Transfer Function

1. Introduction

Orbital CT is a mainstay in routine clinical practice for evaluating trauma (e.g., orbital wall fractures), orbital tumors, inflammatory conditions (e.g., thyroid-associated ophthalmopathy and orbital cellulitis), and for preoperative planning of orbital surgery [1–3]. The orbit consists of the globe and its adnexal soft tissues (including the lens, vitreous body, retina, extraocular muscles, lacrimal gland, optic nerve, and neurovascular bundles) enclosed by dense bony orbital walls [4]. The pronounced attenuation differences between delicate soft tissues and high-density cortical bone render orbital CT prone to beam-hardening and photon-starvation – related artifacts under routine scanning conditions, manifesting as streak artifacts or regional signal loss, which may compromise soft-tissue contrast and the depiction of fine osseous details. Meanwhile, the orbit is a superficial anatomical region that contains the radiosensitive lens, and excessive ionizing radiation may increase the risk of lens opacities and cataract formation [5]. Therefore, optimization of orbital CT protocols requires balancing artifact suppression and diagnostic image quality with stringent radiation dose control.

To address these challenges, prior studies and clinical practice have proposed a range of optimization strategies at both the acquisition-parameter and reconstruction levels. First, for dose control, Organ-based tube current modulation (OBTCM) reduces anteriorly incident dose by lowering the tube current over a predefined anterior angular range, thereby primarily redistributing dose rather than

altering the x-ray spectrum [6]. Because it is fundamentally an mA modulation strategy designed for noise/dose management, OBTCM is not intended as a primary measure for correcting beam-hardening mechanisms, and photon-starvation–related artifacts may still persist under certain conditions [7]. Bismuth eye shielding can reduce lens dose; however, it may increase image noise, introduce streak artifacts, and bias CT numbers, and its performance may vary when combined with automatic exposure control, warranting careful consideration of image-quality trade-offs [8-9]. Second, with respect to image quality, iterative reconstruction and deep-learning–based reconstruction can improve dose efficiency by suppressing noise [10], thereby enabling low-dose protocols, and have demonstrated diagnostic acceptability in high-resolution applications such as paranasal sinus and temporal bone CT [11-12]. However, at ultra-low dose levels or when higher-strength iterative/deep-learning reconstruction is applied, images may exhibit over-smoothing, reduced spatial resolution, and altered noise texture, which can compromise edge sharpness and conspicuity of fine osseous structures, particularly thin cortical bone [13]. Meanwhile, algorithmic “retexturing” of noise and image appearance may also affect the perceived fidelity of soft-tissue structures, with a potential risk of introducing spurious features or obscuring subtle findings [14]. Overall, existing approaches can provide benefits in either dose reduction or image quality, but in orbital CT—where adequate soft-tissue contrast, depiction of fine bony detail, and stringent lens dose control are all required—trade-offs often remain, underscoring the need for more robust strategies that can jointly

optimize these competing demands.

Dual-source spectral shaping (DSSS) has demonstrated advantages in multiple CT applications—including head and neck, paranasal sinus, and chest imaging—by improving image quality while controlling radiation dose [15–21]. The underlying principle of DSSS is spectral shaping to produce a harder X-ray beam, thereby reducing the fraction of low-energy photons that contribute little to image formation [21]. First, because low-energy photons are more readily absorbed in superficial tissues, only a limited proportion reaches the detector and contributes to useful signal; reducing the low-energy component can therefore improve photon utilization efficiency and provide potential for dose reduction to superficial radiosensitive organs [17-19]. Second, spectral hardening increases the mean photon energy and penetration, mitigating photon starvation along high-attenuation paths and consequently reducing beam-hardening– and photon-starvation–related streak artifacts or regional signal loss, while improving the stability of cortical bone delineation [19-21]. On this basis, we hypothesize that DSSS may offer dual benefits in orbital CT: attenuating hardening/starvation artifacts adjacent to the dense orbital walls, while reducing overall radiation exposure at diagnostically acceptable noise levels—particularly in examinations where stringent lens dose control is required.

Given the limited study of DSSS in orbital CT, this study aims to evaluate the effectiveness of DSSS in orbital imaging through phantom experiments and clinical investigations. The aim is to test the above hypothesis and to provide evidence to inform the development of a more optimized orbital CT protocol.

2. Materials and Methods

2.1. Phantom study

2.1.1. Phantom acquisitions

The head diagnostic phantom Model 711-HN (CIRS, USA) and the Catphan (CTP) 600 phantom were scanned using the Siemens Force CT. For the conventional protocol (Group A), the scanning parameters were as follows: tube voltage, 120 kV; tube current, 200 mAs, rotation time, 1.0 s; pitch, 0.8; beam collimation, 192×0.6 mm. Acquisitions were performed at a dose level of 28.4 mGy, which corresponds to the typical radiation dose for an orbital CT examination at the author’s institution. For the DSSS protocol, the tube voltages were set at 100/150 kV (Sn). The tube current was adjusted to ensure that the volume CT dose index ($CTDI_{vol}$) for Group B was similar to that of Group A, while the $CTDI_{vol}$ for Group C was set to 84% of that of Group A. This reduction in $CTDI_{vol}$ for Group C (by 16%) was implemented to compensate for the increased dose-length product (DLP) caused by the dual-source overranging, ensuring that the DLP for Groups A and C remained comparable. All other parameters were kept the same as the conventional protocol. Each of the three groups was scanned ten times.

2.1.2. lens dose measurement

The head diagnostic phantom was used to measure the lens dose, with an imaging range of 8.25 cm.

Thermoluminescent dosimeters (TLDs) were placed at the positions of the bilateral ocular lenses, with two TLDs placed on each side to measure the organ dose of the lenses (Fig. 1A). The lower detection limit of the TLD is 0.004 mGy. The detection instrument used was the BIRM 2000 thermoluminescence dosimeter, with a correction factor of 0.91.

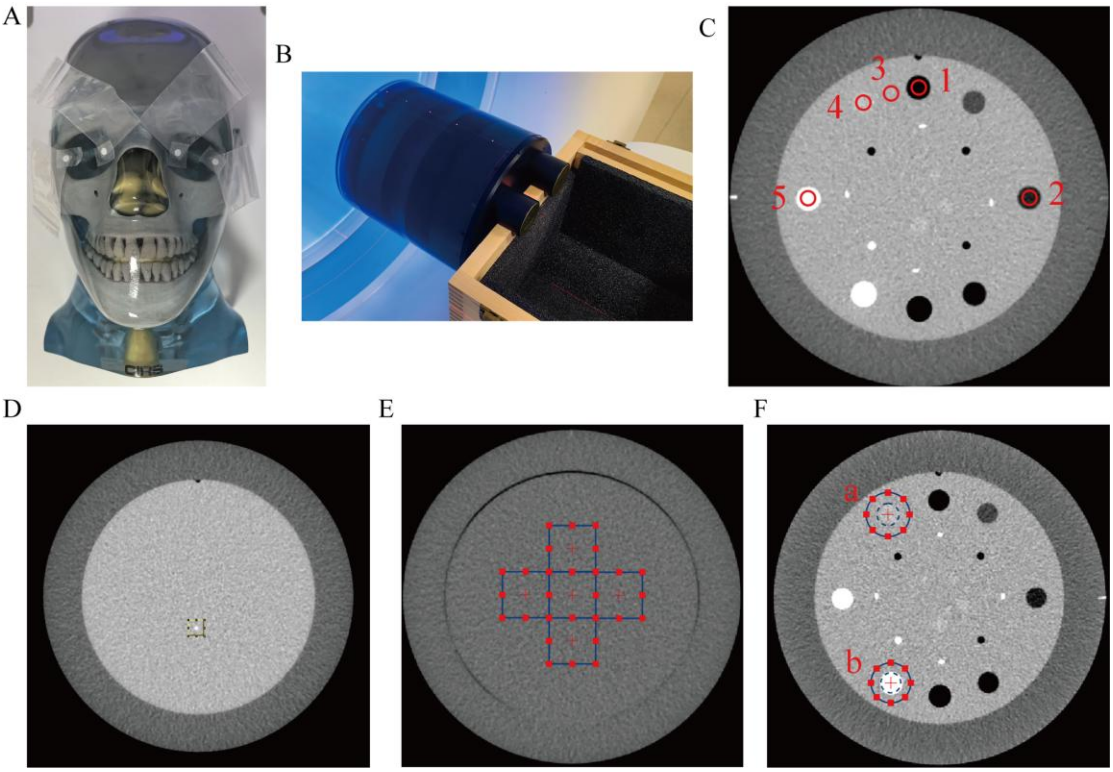


Fig. 1 Schematic diagrams of phantom experiment measurements. a showed the measurement of lens dose using TLD. b showed the placement of Catphan 600 phantom. c showed the measurement of CT values using the CTP404 module. "1" - "5" represent the measured values of CT_1 - CT_5 respectively. d showed the measurement of MTF using the CTP528 module. e showed the measurement of NPS using the CTP486 module. f showed the measurement of TTF using the CTP404 module. "a" is the acrylic

insert and "b" is the bone insert.

2.1.3. Phantom image analysis

The Catphan 600 was used for the evaluation of image quality. The reconstruction parameters were as follows: slice thickness and the slice interval were configured as 0.6 mm. The matrix was 512×512 with FOV of 180 mm, and the ADMIRE level was set at 3. The dual energy scanning parameters were applied to reconstruct the mixed-energy images (DE 0.5). Transverse images were respectively reconstructed using the standard algorithm with the convolutional kernel Hr40 and the bone algorithm with the convolutional kernel Hr59. According to the technical configuration of Siemens SOMATOM Force CT system, the Hr40 kernel provides a medium-sharp reconstruction suitable for orbital soft tissue structures, whereas the Hr59 kernel emphasizes high spatial resolution for bony details, albeit with increased image noise. The methods for image quality evaluation are as follows: (1) CT value: select the central slice of the CTP404 module, and use the Syngo.via workstation to measure the CT values of 5 regions of interest within the slice (Fig. 1C). (2) Modulation Transfer Function (MTF): Select the image of the central slice of the tungsten beads in the CTP528 module. Use Image J to measure the $MTF_{10\%}$ and $MTF_{50\%}$ in the xy plane (Fig. 1D), which are used to represent the high-contrast resolution. (3) Noise Power Spectrum (NPS): Select 5 consecutive slices of images at the center of the CTP486 module, and use the imQuest software to measure the NPS peak and the NPS

average spatial frequency (Fig. 1E). (4) Task Transfer Function (TTF): Select 5 consecutive slices of images at the center of the CTP404 module. Use the imQuest software to measure the $TTF_{50\%}$ of acrylic resin (low-contrast insert, ≈ 120 HU at 120 kVp) and bone (high-contrast insert, ≈ 955 HU at 120 kVp). The region of interest for the image generated with the Hr40 kernel is the acrylic resin insert, whereas the bone insert is designated as the region of interest for the image generated with the Hr59 kernel (Fig. 1F). (5) Detectability Index (d′) [22]: The TTF and NPS were combined to estimate d′ as a function of $CTDI_{vol}$. For the Hr40 task, d′ was calculated using a 3-mm diameter circular signal to simulate the detection of small soft-tissue lesions such as ocular tumors. For the Hr59 task, d′ was calculated using a 1.5-mm diameter circular signal to simulate the identification of fine bony structures, such as orbital bone boundaries. The TTF results derived from acrylic resin and bone materials were applied respectively to represent the soft-tissue (Hr40) and bony (Hr59) imaging characteristics.

The calculation was performed using the Non-Prewhitening with Eye filter (NPWE) observer model, which accounts for the human visual system's frequency response and thereby provides a closer approximation to actual observer performance. In this calculation, the parameter settings for d′ estimation included a zoom factor of 1.5, a viewing distance of 500 mm, and a field of view of 250 mm. A higher d′ value indicates improved detectability of simulated lesions by the observer. The d′ value was calculated using Formula 1.

$$d'_{NPWE} = \left[\iint \frac{|M(u,\upsilon)\, W_{task}(u,\upsilon)\, TTF(u,\upsilon)|^2}{NPS(u,\upsilon)} du\, d\upsilon\right]^{1/2} \quad \text{Eq.(1)}$$

where $W_{task}(u, \upsilon)$ is the Fourier transform of the circular detection task (diameter 3 mm for Hr40; 1.5 mm for Hr59), *TTF* is the task transfer function (measured with acrylic resin for soft tissue and bone for bony characteristics), and *NPS* is the noise power spectrum. $M(u, \upsilon)$ denotes the human-visual-system (eye) filter (visual modulation transfer function) specified for a zoom factor of 1.5, viewing distance of 500 mm, and field of view of 250 mm. A higher d' indicates better detectability.

2.2. Clinical study

2.2.1. Study Population

This study enrolled 85 patients who underwent DSSS orbital CT and 78 patients who underwent conventional orbital CT at our institution between November 2024 and February 2025. The inclusion criteria were: age ≥ 18 years. The exclusion criteria were as follows: (1) obvious motion artifacts in the eyeballs (n = 1), and (2) lack of TLD measurement values (n = 2). Ultimately, the conventional group consisted of 40 males and 35 females, aged 18 - 74 years, with a mean age of 42.6±14.5 years. The DSSS group included of 43 males and 42 females, aged 19 - 86 years, with a mean age of 48.2±14.7 years. This study was approved by the Ethics committee (TREC2025-KY041).

2.2.2. Data acquisitions

The scanning method for the conventional group followed the same protocol as Group A in the phantom experiments, while the DSSS group adhered to the protocol of Group C. The scanning range extended from the upper to the lower orbital margin. All other parameters were consistent with those of the phantom experiments.

2.2.3. Dose measurement

Two TLDs were attached to the inner surface of the eye mask to estimate the lens dose, with the lens dose calculated as the average of the two sides. The $CTDI_{vol}$ and DLP for all patients were recorded.

2.2.4. Quantitative image analysis

The cross-sectional soft tissue algorithm image (Hr40) of the eyeball’s maximum diameter line was selected. The following steps were performed: (1) The medial rectus muscle and the eyeball were considered as the signal areas, with fat serving as the background area. Circular regions of interest (ROIs) of approximately $3mm^2$ were drawn in each area to measure the CT value and standard deviation (SD) (Fig. 2A). The contrast-to-noise ratio (CNR) was then calculated using Formula 2.

$$\mathrm{CNR} = \frac{\mathrm{CT_1} - \mathrm{CT_2}}{\sqrt{\frac{\mathrm{SD_1^2} + \mathrm{SD_2^2}}{2}}} \qquad \text{Eq.(2)}$$

Here, CT_1 and SD_1 represent the CT value and SD of the signal areas (eyeball or medial rectus muscle), while CT_2 and SD_2 represent those of the background area (fat).

(2) A rectangular ROI was delineated within the vitreous cavity to maximize coverage while excluding the lens and scleral structures. On the original images (with no median or Gaussian preprocessing), the

gray-scale standard deviation (SD, HU) within the ROI was computed using an in-house MATLAB script to quantify streak/beam-hardening artifacts (Fig. 2B). Although this noise-inclusive SD is influenced by random noise as well as artifacts, lower values generally indicate fewer artifacts; accordingly, the potential impact of noise was considered when interpreting the results.

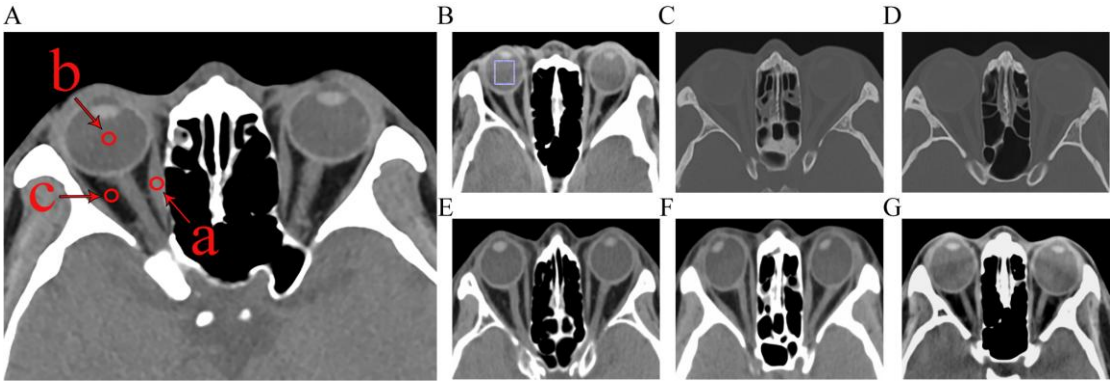


Fig. 2 Schematic diagrams of clinical research measurements. In a, a, b, and c represent the medial rectus muscle, eyeball, and fat, respectively. b showed the measurement of the gray - scale standard deviation using Matlab. c and d are diagrams of bone algorithm(Hr59) scores of 5 and 4 points, respectively. e - g are diagrams of standard algorithm(Hr40) scores of 5, 4, and 3 points, respectively.

2.2.5. Qualitative image analysis

Two senior radiologists (12 and 15 years of CT diagnostic experience, respectively) evaluated the images(Hr40 and Hr59) using a double-blind method. The scoring criteria were determined based on a comprehensive assessment of image clarity and the impact of artifacts on diagnosis. For soft

tissue(Hr40), the evaluation focused on the fat, scleral ring, lens, vitreous body, optic nerve, and extraocular muscles. For bone(Hr59), the margins of the orbital bones, fracture lines, and fracture ends were emphasized. The scoring criteria were as follows: 5 = Extremely clear structural details and lesions, with no beam-hardening artifact (Fig. 2C, E); 4 = Relatively clear structural details and lesions, with either no beam- hardening artifact or mild artifact that does not impede the observation of structures/lesions (Fig. 2D, F); 3 = Relatively clear display of most structural details and lesions, with mild beam-hardening artifacts slightly affecting local detail observation, but still suitable for diagnosis(Fig. 2G); 2 = Obvious beam-hardening artifact, affecting observation of some structural details and lesions; 1 = Poor visibility of structural details and lesions, with prominent beam-hardening artifact.

2.3. Statistical analysis

Statistical analysis was performed using SPSS (version 26.0). Data were presented as mean ± standard deviation for normally distributed variables and as median (interquartile range, IQR) for non-normally distributed variables. For the phantom study, a one-way analysis of variance was conducted to compare the lens doses among the three groups(Group A, B, C) and to evaluate image quality parameters of the Catphan 600 phantom. Statistical significance was defined as $P < 0.05$, and when this threshold was met, the Least Significant Difference method was applied for post hoc pairwise group comparisons. Additionally, an interrater reliability analysis was performed to calculate the Kappa value, with a

consistency level of 0.8 to 1.0 considered very strong.

3. Results

3.1. Phantom study

3.1.1. lens dose measurement

The scanning parameters and doses for groups A, B and C are presented in Table 1 and Fig. 3A. The lens dose in group C was significantly lower compare to that in groups A and B.

Table 1 Phantom scanning parameters and radiation dose results

Group	Tube voltage （kV）	Tube current （mAs）	$CTDI_{vol}$ （mGy）	DLP （mGy • cm）	Scanning length （cm）	Dose of the lens （mGy）
A	120	200	28.38	321.8	11.34	19.71±1.46[C]
B	100/Sn150	232/145	28.32	380.3	13.42	20.62±1.11[C]
C	100/Sn150	195/122	23.78	319.2	13.42	17.50±0.91
F	—	—	—	—	—	9.220
P	—	—	—	—	—	0.004

Group A is the conventional group. Groups B(same $CTDI_{vol}$ as Group A) and C(84% $CTDI_{vol}$ as Group A) are the dual-source spectral shaping groups. $CTDI_{vol}$：Volume CT dose index. DLP：Dose Length

Product.

Post hoc pairwise comparisons using the the Least Significant Difference test revealed significant differences ($P < 0.05$) in means compared to Group C([C]).

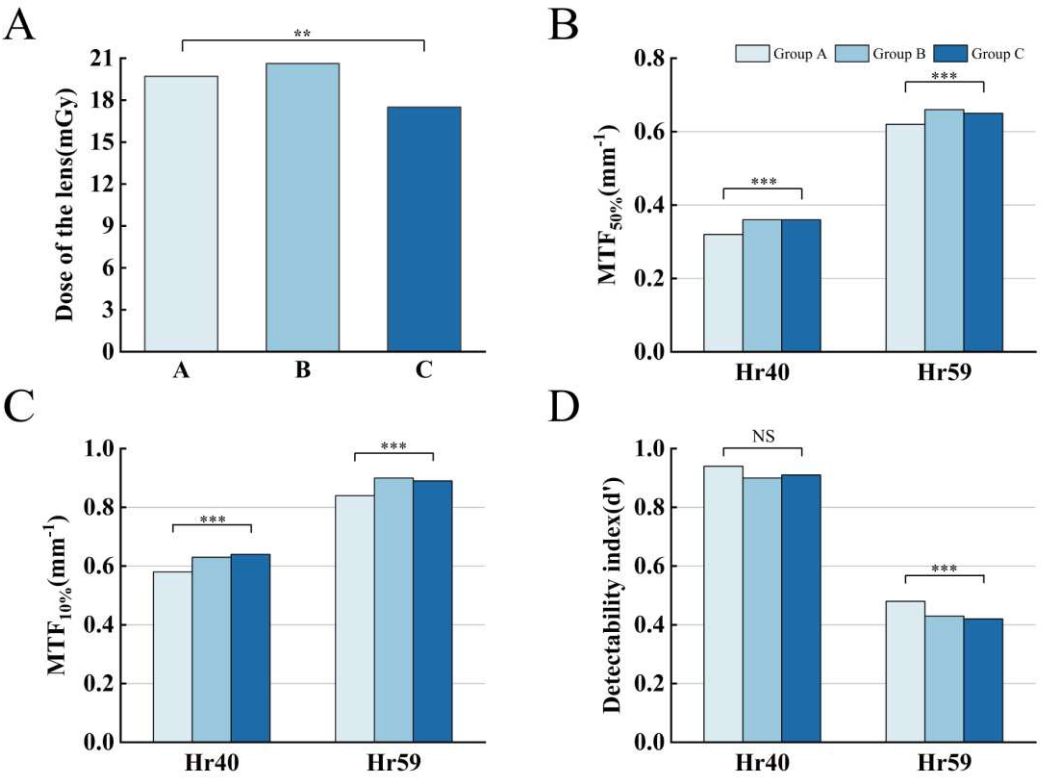


Fig. 3 Phantom study result. a showed the average lens dose of groups A, B, and C. b - d showed the average values of $MTF_{50\%}$, $MTF_{10\%}$, and d' for groups A, B, and C under two filter kernels respectively.

3.1.2. image quality assessment

The CT values of the images for groups A, B and C, along with the image quality assessment, are

shown in Tables 2 and 3, and illustrated in Figs. 3 and 4. Except for CT_4, the CT values for groups B and C differed significantly from those of group A ($P < 0.001$). The $MTF_{50\%}$ and $MTF_{10\%}$ for groups B and C were significantly higher than those for group A ($P < 0.001$). No significant difference was found in the d' value for Hr40 among the three groups ($P = 0.830$). However, the d′ value for Hr59 in group A was significantly higher than that in groups B and C ($P < 0.001$).

Table 2 CT value of phantom scanning image

Group	CT_1（HU）	CT_2（HU）	CT_3（HU）	CT_4（HU）	CT_5（HU）
A	-1022.77±0.24^{BC}	-123.31±1.76^{BC}	105.59±1.40^{BC}	128.24±1.30	395.13±1.56^{BC}
B	-973.88±1.99	-84.22±1.49	102.46±1.61	127.71±1.50	345.48±1.87
C	-973.56±1.24	-83.74±1.79	103.13±0.88	126.93±1.74	346.04±1.21
F	4332.409	1618.488	15.300	1.872	3277.137
P	<0.001	<0.001	<0.001	0.173	<0.001

Group A is the conventional group. Groups B(same $CTDI_{vol}$ as Group A) and C(84% $CTDI_{vol}$ as Group A) are the dual-source spectral shaping groups.

Post hoc pairwise multiple comparisons procedure with the Least Significant Difference test showed a statistically significant ($P < 0.05$) difference between means when compared with B (^{B}) and C(^{C}).

Table 3 image quality by Phantom scanning

convolutional kernel	Group	$MTF_{50\%}$ (mm^{-1})	$MTF_{10\%}$ (mm^{-1})	NPS peak ($HU^2 \cdot mm^2$)	NPS average spatial frequency (mm^{-1})	$TTF_{50\%}$ (acrylic inserts) (mm^{-1})	$TTF_{50\%}$ （bone） (mm^{-1})	d’
Hr 40	A	0.32±0.01[BC]	0.58±0.01[BC]	235.42±0.01[BC]	0.28±0.01	0.39±0.08	—	0.94±0.10
	B	0.36±0.01	0.63±0.01	229.66±7.86[C]	0.28±0.01	0.38±0.09	—	0.90±0.13
	C	0.36±0.01	0.64±0.01	271.91±0.01	0.28±0.01	0.46±0.10	—	0.91±0.17
	F	58.952	76.339	75.764	0.122	2.266	—	0.188
	P	<0.001	<0.001	<0.001	0.886	0.123	—	0.830
Hr 59	A	0.62±0.01[BC]	0.84±0.01[BC]	732.95±10.22[BC]	0.56±0.00[BC]	—	1.44±0.03[BC]	0.48±0.01[BC]
	B	0.66±0.01	0.90±0.01	829.10±15.76[C]	0.55±0.00	—	1.60±0.05[C]	0.43±0.01
	C	0.65±0.01	0.89±0.02	974.21±19.65	0.55±0.00	—	1.78±0.07	0.42±0.01
	F	22.249	55.009	690.958	36.500	—	35.041	87.399

P	<0.001	<0.001	<0.001	<0.001	—	<0.001	<0.001

Group A is the conventional group. Groups B(same $CTDI_{vol}$ as Group A) and C(84% $CTDI_{vol}$ as Group A) are the dual-source spectral shaping groups.

Post hoc pairwise multiple comparisons procedure with the Least Significant Difference test showed a statistically significant ($P < 0.05$) difference between means when compared with B (^{B}) and C(^{C}).

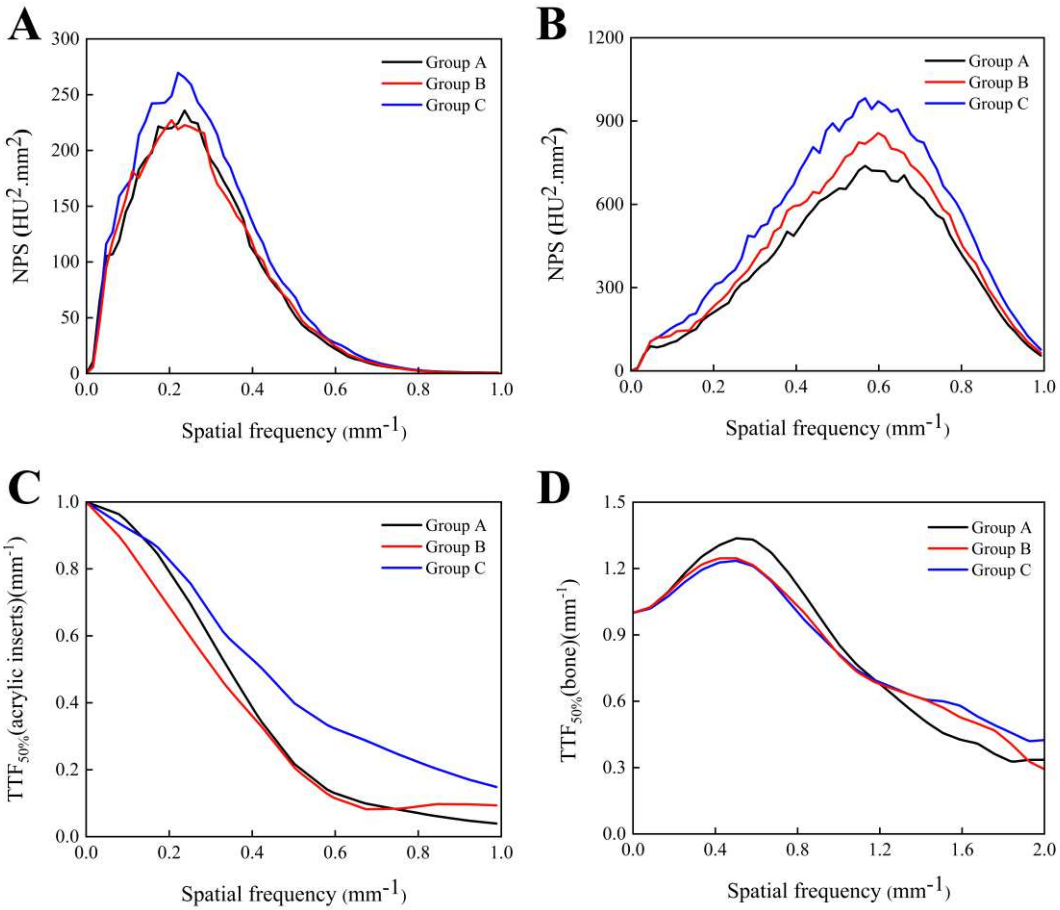


Fig. 4 Noise power spectrum (NPS) and task transfer function (TTF) results for groups A, B, and C using images reconstructed with the Hr40 and Hr59 kernels.

3.2. Clinical study

3.2.1. Dose measurement

The patient dose data are summarized in Table 4 and illustrated in Fig. 5. There was no statistically significant difference in the DLP between the two groups. However, both the scan length and lens dose showed significant differences ($P < 0.001$), with the DSSS group demonstrating a significantly lower lens dose compared to the conventional group.

Table 4 Radiation dose in clinical study

Group	$CTDI_{vol}$（mGy）	DLP（mGy·cm）	Scanning length（cm）	Dose of the lens（mGy）
Con	28.38	304.90(293.50，324.70)	10.74(10.34，11.44)	20.10(17.93，22.68)
DSSS	23.78	307.21(289.08，325.31)	12.92(12.16，13.70)	17.35(15.85，18.82)
Z	—	-0.488	-8.983	-5.818
P	—	0.626	<0.001	<0.001

Con, conventional group; DSSS, dual-source spectral shaping group; $CTDI_{vol}$, Volume CT dose index; DLP, Dose Length Product.

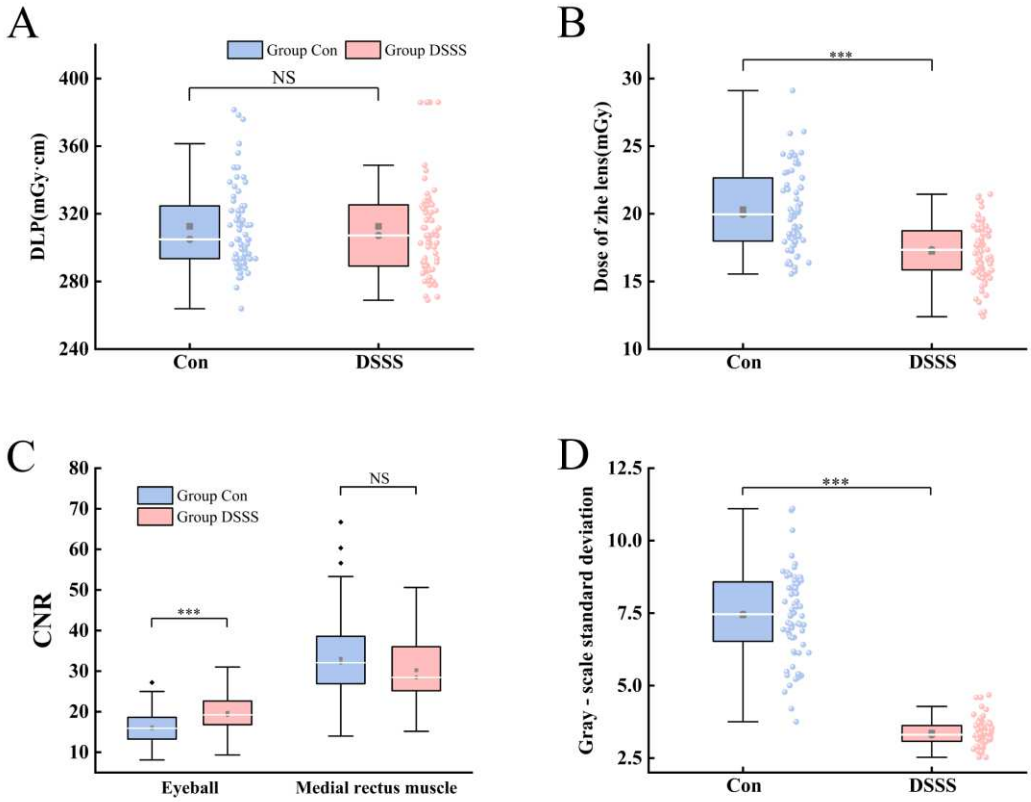


Fig. 5 Clinical study result. A - D showed the DLP, lens dose, CNR, and gray - scale standard deviation of the conventional group(Con) and dual-source spectral shaping group(DSSS), respectively.

3.2.2. Quantitative image analysis

The results of the quantitative measurements are shown in Table 5 and illustrated in Fig. 5. No significant difference was observed in the CNR of the medial rectus muscle between the two groups. The CNR of the eyeball in the DSSS group was significantly higher than in the conventional group, while the gray - scale standard deviation showed the opposite trend ($P < 0.001$).

Table 5 Image quality in clinical study

Group	$CT_{medial\ rectus\ muscle}$ （HU）	$CT_{eyeball}$ （HU）	CT_{fat} （HU）	$CNR_{medial\ rectus\ muscle}$	$CNR_{eyeball}$	gray - scale standard deviation
Con	83.18±14.10	27.00 (22.00，30.00)	-104.32±10.01	33.10±10.34	16.11±3.86	7.44±1.53
DSSS	43.27±5.80	2.00 (0.00，4.00)	-86.44±7.69	30.26±7.55	19.77±4.15	3.36±0.45
t	-22.888		12.189	-1.909	5.493	-22.521
Z		-10.422				
P	<0.001	<0.001	<0.001	0.058	<0.001	<0.001

Con, conventional group; DSSS, dual-source spectral shaping group.

$CNR_{medial\ rectus\ muscle}$ and $CNR_{eyeball}$ are the CNR values calculated by using the medial rectus muscle and the eyeball as the signal regions, respectively, and fat as the background region.

3.2.3. Qualitative image analysis

Interobserver agreement between the two radiologists was good, with κ values $\geqslant$0.75 for all qualitative assessments (Table 6). The overall image quality for Hr40 image in the DSSS group was superior to that in the conventional group. In terms of score distribution, the DSSS group showed an

upward trend in scores compared to the conventional group, with an increased proportion of grade 5 scores and no images rated as grade 3. The overall distribution of Hr59 image quality showed little change. Fig. 6 displays the images of the same patient scanned by the two scanning methods, highlighting the differences in image quality.

Table 6 image quality evaluation by two radiologists and consistency analysis

	image quality evaluation				consistency analysis					
	Hr40		Hr59		Hr40			Hr59		
	Reader 1	Reader 2	Reader 1	Reader 2	Reader 1	Reader 2	*Kappa*	Reader 1	Reader 2	*Kappa*
Con	5(13)* 4(54)* 3(8)*	5(14)* 4(53)* 3(8)*	5(70)* 4(5)*	5(71)* 4(4)*	4.0 （4.0， 4.0）	4.0 （4.0， 4.0）	0.891	5.0 （5.0， 5.0）	5.0 （5.0， 5.0）	0.878
DSSS	5(58)* 4(25)* 3(2)*	5(56)* 4(28)* 3(1)*	5(79)* 4(6)*	5(79)* 4(6)*	5.0 （4.0， 5.0）	5.0 （4.0， 5.0）	0.870	5.0 （5.0， 5.0）	5.0 （5.0， 5.0）	0.873

* The number in parentheses is the number of patients.

Con, conventional group; DSSS, dual-source spectral shaping group.

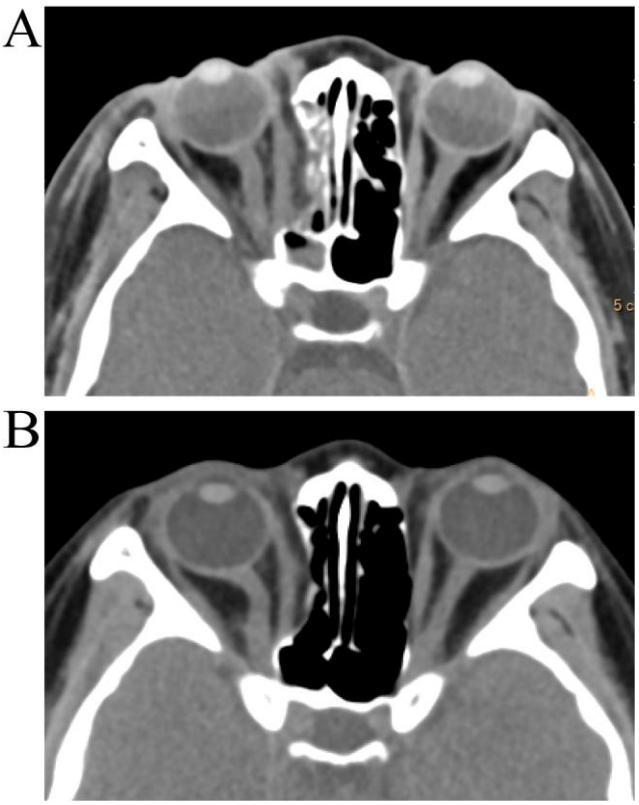


Fig. 6 Effect images of the same patient scanned by two methods.

A and B are images of the same patient obtained by conventional scanning and dual-source spectral shaping technology, respectively.

4. Discussion

This study evaluated the application of DSSS technology in orbital CT through phantom experiments and clinical research. The results showed that in the phantom experiments, DSSS (Group C, with DLP comparable to the conventional protocol) significantly improved high-contrast resolution and reduced lens dose, without affecting image d′ (Hr40). Clinical research further verified that DSSS can reduce eye lens dose by approximately 14%, while significantly enhancing image quality and reducing

beam-hardening artifacts.

In both the conventional and dual-source spectral shaping scanning protocols of this study, a fixed tube current was selected instead of automatic modulation techniques. This decision was based on the anatomical characteristics of the orbital region. In adults, the head size at the orbital level is relatively consistent, and the orbit does not contain gas or other tissues with low X-ray attenuation. According to expert consensus[4], the use of automatic exposure modulation is not recommended for orbital CT scans. In this study, the $CTDI_{vol}$ in the conventional group was approximately 29% lower than the diagnostic reference level, and the $CTDI_{vol}$ in the low-dose DSSS group (Group C) was below the "achievable dose" level of 25 mGy. Therefore, this study placed strong emphasis on minimizing radiation exposure to the lens, with dose reduction as a primary objective. Phantom experiments and clinical studies were conducted to verify the feasibility of the DSSS technique. This study evaluated DSSS under two comparison frameworks: Group B and Group C. The former was used to assess the impact of system geometry/over-ranging on DLP, while the latter was employed to evaluate the organ dose and image quality benefits under the condition of comparable overall exposure.

The phantom experiments in this study revealed that, under identical $CTDI_{vol}$ conditions, there was no statistically significant difference in lens dose between the DSSS group and the conventional group. However, the DLP increased by approximately 18% in the DSSS group. This increase can be attributed to the nature of CT image reconstruction, wherein interpolation algorithms require data acquisition

beyond the planned scan range. This necessitates scanning of tissues beyond the target region, resulting in a phenomenon known as z-axis overranging[23]. Notably, the dual-source configuration used in this study involves two X-ray tubes positioned at a 95°angle [24]. Compared to single-source systems, this geometry increases the extent of overranging during helical acquisition. The actual scan length in the DSSS protocol was approximately 2 cm longer than in the conventional setup, contributing to the higher DLP. To offset this increase, the $CTDI_{vol}$ in the DSSS group (Group C) was reduced to 84% of that in the conventional group. As a result, the DLP remained comparable between the two protocols, suggesting similar overall exposure and serving as a comparable surrogate for effective dose. Under these matched DLP conditions, DSSS achieved a 16% reduction in $CTDI_{vol}$ and an 11% reduction in lens dose. Significant differences in CT values were observed among the groups. This finding is consistent with previous studies[25]: DSSS can lead to shifts in absolute CT attenuation values; however, the relative contrast between tissues generally remains stable, thereby preserving the reliability of clinical interpretation. Nevertheless, caution should be exercised when performing quantitative analyses based on HU values, such as thresholding or cross-protocol and cross-system comparisons. Additionally, NPS peak was elevated, whereas the mean spatial frequency of the NPS showed no significant difference; this finding is consistent with Greffier et al. [20], indicating that DSSS does not alter the intrinsic noise texture of CT images. At the same time, increases in $MTF_{50\%}$, $MTF_{10\%}$, and $TTF_{50\%}$ demonstrated that DSSS enhanced spatial resolution and signal transfer across

multiple frequency ranges, thereby improving contrast and edge definition, with particular benefits for the depiction of bony structures using the bone reconstruction algorithm [19]. The observed $TTF_{50\%}$ can be explained by imaging physics and reconstruction parameters: first, spectral shaping with a tin filter reduces beam-hardening artifacts and streaks, increases local gray-level gradients, and facilitates the transfer of low- to mid-frequency information[25]; second, the ADMIRE iterative reconstruction algorithm suppresses noise while preserving edge sharpness, thereby further supporting edge transfer [26]. Together, these factors resulted in a marked improvement of $TTF_{50\%}$ in Group C. Under the Hr40 kernel, no significant differences in d′ were observed among the three groups; however, under Hr59 kernel, the d′ of Group C was significantly lower than that of Group A, suggesting that DSSS imposes certain limitations on the transfer of high-frequency information, while exerting no apparent effect on low- or mid-frequency transfer. High-frequency components primarily correspond to small, high-contrast structures, such as ultra-fine osseous details, whereas overall bone continuity relies more heavily on low- and mid- frequency information that defines general contours and edges, and does not depend entirely on the finest high-frequency elements [27]. Accordingly, the reduction in d′ observed in this study mainly reflects impaired d’ of fine osseous details. Nevertheless, as most orbital CT examinations in clinical practice depend on accurate visualization of soft tissues and assessment of overall bone continuity rather than ultra-fine osseous details [3], the clinical impact of this limitation is expected to be minimal.

The clinical validation further supported the phantom results, confirming that the low-$CTDI_{vol}$ DSSS protocol reduced lens radiation dose by approximately 14% with no significant difference in DLP. In standard algorithm reconstructions, the CNR— with the eyeball as the signal region and periorbital fat as the background—increased by about 23%, indicating a notable enhancement in low-contrast resolution. Moreover, the grayscale standard deviation within the eyeball decreased by 55%, substantially reducing intraocular artifacts. Subjective image quality scores were highly consistent with objective measurements. The DSSS group received higher overall ratings than the conventional group, with the greatest improvement seen in standard reconstruction images. Radiologists reported a markedly improved visualization of the scleral ring, lens, and vitreous body, due to a significant reduction in beam-hardening artifacts. These clinical observations are consistent with those reported by Zhou, W. [17], and further validated by Lee, S. M. [21], who demonstrated that DSSS effectively reduces beam-hardening artifacts without increasing radiation exposure.

Nevertheless, this study has several limitations. First, DSSS showed a reduced d′ for fine osseous details with the Hr59 kernel relative to the conventional protocol, suggesting limited transfer of high-frequency information. Second, the direct impact of DSSS on the diagnostic performance of specific orbital diseases was not assessed. Third, only 0.5 mixed-energy images were evaluated, without investigating other blending ratios or energy levels that might offer further optimization. Fourth, the DSSS technique is currently restricted to dual-source CT systems, limiting its applicability

across different scanner platforms. Fifth, the MTF reported in this study were derived from images reconstructed with ADMIRE (strength 3). Since $MTF_{50\%}$ and $MTF_{10\%}$ is reconstruction-dependent, its values and frequency responses vary with the reconstruction method; therefore, the present results should be regarded only as secondary references. Finally, because DSSS may shift absolute CT attenuation values, HU-based quantitative analyses (e.g., thresholding or cross-protocol comparisons) should be interpreted with caution. Future investigations should further explore whether spectral shaping with customized energy parameters can enhance diagnostic accuracy in orbital imaging while maintaining or further reducing radiation dose.

5. Conclusion

Clinical validation showed that dual-source spectral shaping reduced lens radiation dose by 14% without increasing DLP, while significantly improving image quality—reflected by a 23% increase in CNR and reduced intraocular artifacts. DSSS offers a promising low-dose solution for orbital CT imaging with maintained diagnostic performance.

References

1. Cellina, M., Cè, M., Marziali, S., Irmici, G., Gibelli, D., Oliva, G., & Carrafiello, G. (2022). Computed tomography in traumatic orbital emergencies: a pictorial essay-imaging findings, tips, and

report flowchart. Insights into imaging, 13(1), 4. https://doi.org/10.1186/s13244-021-01142-y

2. Ferreira, T. A., Saraiva, P., Genders, S. W., Buchem, M. V., Luyten, G. P. M., & Beenakker, J. W. (2018). CT and MR imaging of orbital inflammation. Neuroradiology, 60(12), 1253–1266. https://doi.org/10.1007/s00234-018-2103-4

3. Betts, A. M., O'Brien, W. T., Davies, B. W., & Youssef, O. H. (2014). A systematic approach to CT evaluation of orbital trauma. Emergency radiology, 21(5), 511–531. https://doi.org/10.1007/s10140-014-1221-5

4. Head and Neck Group of Chinese Society of Radiology Chinese Medical Association, Radiation Protection Group of Chinese Society of Imaging Technology Chinese Medical Association. Expert consensus on head and neck CT examination and radiation dose management.Chinese Journal of Radiology.2020, 54(09)：827-838, https://doi.org/10.3760/cma.j.cn112149-20200424-00608.

5. Worgul, B. V., Kundiyev, Y. I., Sergiyenko, N. M., et al. Cataracts among Chernobyl clean-up workers: implications regarding permissible eye exposures. Radiation research, 2007, 167(2), 233–243. https://doi.org/10.1667/rr0298.1.

6. Papadakis AE, Damilakis J. Evaluation of an organ-based tube current modulation tool in pediatric CT examinations. Eur Radiol. 2020 Oct;30(10):5728-5737. doi: 10.1007/s00330-020-06888-5.

7. Duan X, Wang J, Christner JA, Leng S, Grant KL, McCollough CH. Dose reduction to anterior surfaces with organ-based tube-current modulation: evaluation of performance in a phantom study. AJR

Am J Roentgenol. 2011 Sep;197(3):689-95. doi: 10.2214/AJR.10.6061.

8. Kalra MK, Dang P, Singh S, Saini S, Shepard JA. In-plane shielding for CT: effect of off-centering, automatic exposure control and shield-to-surface distance. Korean J Radiol. 2009 Mar-Apr;10(2):156-63. doi: 10.3348/kjr.2009.10.2.156.

9. Wang J, Duan X, Christner JA, Leng S, Grant KL, McCollough CH. Bismuth shielding, organ-based tube current modulation, and global reduction of tube current for dose reduction to the eye at head CT. Radiology. 2012 Jan;262(1):191-8. doi: 10.1148/radiol.11110470.

10. Cheng, Y., Ma, Z., Guo, S., Xu, C., Liu, D., & Zhang, Y. (2025). Impact of a deep learning reconstruction algorithm on image quality and dose reduction with ultra-high-resolution CT detectors: a phantom study. Zeitschrift fur medizinische Physik, S0939-3889(25)00152-7. Advance online publication. https://doi.org/10.1016/j.zemedi.2025.11.002.

11. Li, Y., Liu, X., Zhuang, X. H., Wang, M. J., & Song, X. F. (2022). Assessment of low-dose paranasal sinus CT imaging using a new deep learning image reconstruction technique in children compared to adaptive statistical iterative reconstruction V (ASiR-V). BMC medical imaging, 22(1), 106. https://doi.org/10.1186/s12880-022-00834-1.

12. Leng S, Diehn FE, Lane JI, Koeller KK, Witte RJ, Carter RE, McCollough CH. Temporal Bone CT: Improved Image Quality and Potential for Decreased Radiation Dose Using an Ultra-High-Resolution Scan Mode with an Iterative Reconstruction Algorithm. AJNR Am J Neuroradiol. 2015

Sep;36(9):1599-603. doi: 10.3174/ajnr.A4338.

13. Hoxworth JM, Lal D, Fletcher GP, Patel AC, He M, Paden RG, Hara AK. Radiation dose reduction in paranasal sinus CT using model-based iterative reconstruction. AJNR Am J Neuroradiol. 2014 Apr;35(4):644-9. doi: 10.3174/ajnr.A3749.

14. Koetzier LR, Mastrodicasa D, Szczykutowicz TP, van der Werf NR, Wang AS, Sandfort V, van der Molen AJ, Fleischmann D, Willemink MJ. Deep Learning Image Reconstruction for CT: Technical Principles and Clinical Prospects. Radiology. 2023 Mar;306(3):e221257. doi: 10.1148/radiol.221257.

15. Suntharalingam, S., Stenzel, E., Wetter, A.,et al. Third generation dual-energy CT with 80/150 Sn kV for head and neck tumor imaging. Acta radiologica (Stockholm, Sweden : 1987). 2019, 60(5), 586–592. https://doi.org/10.1177/0284185118788896.

16. Luo, S., Sha, Y., Wu, J., et al. Differentiation of malignant from benign orbital tumours using dual-energy CT. Clinical radiology. 2022, 77(4), 307–313. https://doi.org/10.1016/j.crad.2021.12.019.

17. Zhou, W., Malave, M. N., Maloney, J. A., et al. Radiation dose reduction using spectral shaping in pediatric non-contrast sinus CT. Pediatric radiology. 2023, 53(10), 2069–2078. https://doi.org/10.1007/s00247-023-05699-2.

18. Takemitsu, M., Takegami, K., Kudomi, S., & Kawanami, K. Patient dose reduction for a localizer radiograph with an additional tin filter in chest-abdomen-pelvis, spine, and head computed tomography examinations. Radiological physics and technology, 2023, 16(2), 160–167.

https://doi.org/10.1007/s12194-023-00701-w.

19. Rehan, S., Kutschera, P., Paul, E., Lau, T., & Lau, K. K. High-pitched tin-filtered CT pulmonary angiography in radiation dose reduction for pulmonary embolism investigations in young females. Emergency radiology. 2023, 30(4), 425–433. https://doi.org/10.1007/s10140-023-02142-9

20. Greffier, J., Fitton, I., Ngoc Ty, C. V., Frandon, J., Beregi, J. P., & Dabli, D. Impact of tin filter on the image quality of ultra-low dose chest CT: A phantom study on three CT systems. Diagnostic and interventional imaging. 2023, 104(10), 506–512. https://doi.org/10.1016/j.diii.2023.05.005.

21. Lee, S. M., Choo, H. J., et al. Cervical Spine CT Using Spectral Shaping: Can It Be a Solution to Overcome Artifacts in the Lower Cervical Spinal Region?. Korean journal of radiology, 2019, 20(3), 469–478. https://doi.org/10.3348/kjr.2018.0517.

22. Samei, E., Bakalyar, D., Boedeker, K. L., Brady, S., Fan, J., Leng, S., Myers, K. J., Popescu, L. M., Ramirez Giraldo, J. C., Ranallo, F., Solomon, J., Vaishnav, J., & Wang, J. (2019). Performance evaluation of computed tomography systems: Summary of AAPM Task Group 233. Medical physics, 46(11), e735–e756. https://doi.org/10.1002/mp.13763

23. Tzedakis, A., Damilakis, J., Perisinakis, K., Stratakis, J., & Gourtsoyiannis, N. The effect of z overscanning on patient effective dose from multidetector helical computed tomography examinations. Medical physics, 2005, 32(6), 1621–1629. https://doi.org/10.1118/1.1924309.

24. Schmidt, B., & Flohr, T. Principles and applications of dual source CT. Physica medica : PM : an

international journal devoted to the applications of physics to medicine and biology : official journal of the Italian Association of Biomedical Physics (AIFB), 2020, 79, 36–46, https://doi.org/10.1016/j.ejmp.2020.10.014.

25. Greffier, J., Pereira, F., Hamard, A., Addala, T., Beregi, J. P., & Frandon, J. (2020). Effect of tin filter-based spectral shaping CT on image quality and radiation dose for routine use on ultralow-dose CT protocols: A phantom study. Diagnostic and interventional imaging, 101(6), 373 – 381. https://doi.org/10.1016/j.diii.2020.01.002

26. Ellmann, S., Kammerer, F., Allmendinger, T., Hammon, M., Janka, R., Lell, M., Uder, M., & Kramer, M. (2018). Advanced Modeled Iterative Reconstruction (ADMIRE) Facilitates Radiation Dose Reduction in Abdominal CT. Academic radiology, 25(10), 1277 – 1284. https://doi.org/10.1016/j.acra.2018.01.014

27. Greffier, J., Hamard, A., Pereira, F., Barrau, C., Pasquier, H., Beregi, J. P., & Frandon, J. (2020). Image quality and dose reduction opportunity of deep learning image reconstruction algorithm for CT: a phantom study. European radiology, 30(7), 3951 – 3959. https://doi.org/10.1007/s00330-020-06724-w

Declarations

Ethics approval and consent to participate

This study was approved by the Ethics Committee of Beijing Tongren Hospital, Capital Medical University (TREC KY2016-003; approval date: March 1, 2016). The study was conducted in accordance with the Declaration of Helsinki and relevant institutional guidelines and regulations. Written informed consent to participate was obtained from all participants prior to enrollment.

Consent for publication

Not applicable.

Availability of data and materials

The datasets used and/or analysed during the current study are available from the corresponding author on reasonable request.

Competing interests

The authors declare that they have no competing interests.

Funding

National Natural Science Foundation of China（82271988）

Authors' contributions

Zixuan Ma: Writing – original draft, Formal analysis.

Zechen Feng: Resources.

Wei Li: Data curation.

Yuhe Cheng: Software.

Wentao Ma: Visualization.

Yongxian Zhang: Project administration.

Yantao Niu: Supervision, Funding acquisition

Dandan Liu: Writing – review & editing, Formal analysis, Data curation.

Acknowledgements

Not applicable.